Scaling up Electronic Spin Qubits into a Three-Dimensional Metal-Organic Framework

Scaling up Electronic Spin Qubits into a Three-Dimensional Metal-Organic Framework

Tsutomu Yamabayashi,[†] Matteo Atzori,[‡] Lorenzo Tesi,[‡] Goulven Cosquer,[†] Fabio Santanni,[‡] Marie-Emmanuelle Boulon,[‡] Elena Morra,[§] Stefano Benci,[∥] Renato Torre,[∥,⊥] Mario Chiesa,[§] Lorenzo Sorace,[‡] Roberta Sessoli[‡,#,*] and Masahiro Yamashita[†,▽,◊,*]

[†] Department of Chemistry, Graduate School of Science, Tohoku University, 6-3 Aramaki Aza-Aoba, Aoba-ku, 980-8578 Sendai, Japan.

[‡] Dipartimento di Chimica "Ugo Schiff" & INSTM RU, Università degli Studi di Firenze, Via della Lastruccia 3, I50019 Sesto Fiorentino (Firenze), Italy.

[§] Dipartimento di Chimica e NIS Centre, Università di Torino, Via P. Giuria 7, I10125 Torino, Italy.

[∥] European Laboratory for Non-Linear Spectroscopy, Università degli Studi di Firenze, Via Nello Carrara 1, I50019 Sesto Fiorentino (Firenze), Italy.

[⊥] Dipartimento di Fisica ed Astronomia, Università degli Studi di Firenze, Via G. Sansone 1, I50019 Sesto Fiorentino (Firenze), Italy.

[#] ICCOM-CNR, Research Area Firenze, Via Madonna del Piano 10, I50019 Sesto Fiorentino (Firenze), Italy.

[▽] WPI, Advanced Institute for Materials Research, Tohoku University, 2-1-1 Katahira, Aoba-Ku, Sendai 980-8577, Japan.

[◊] School of Materials Science and Engineering, Nankai University, Tianjin 300350, China.

ABSTRACT: Practical implementation of highly coherent molecular spin qubits for challenging technological applications, such as quantum information processing or quantum sensing, requires precise organization of electronic qubit molecular components into extended frameworks. Realization of spatial control over qubit-qubit distances can be achieved by coordination chemistry approaches through an appropriate choice of the molecular building blocks. However, translating single qubit molecular building units into extended arrays does not guarantee *a priori* retention of long quantum coherence and spin-lattice relaxation times due to the introduced modifications over qubit-qubit reciprocal distances and molecular crystal lattice phonons structure. In this work, we report the preparation of a three-dimensional (3D) metal-organic framework (MOF) based on vanadyl qubits, [VO(TCPP-Zn_2-bpy)] (TCPP = tetracarboxyl-phenylporphyrinate; bpy = 4,4'-bipyridyl) (**1**), and the investigation of how such structural modifications influence qubits performances. This has been done through a multitechnique approach where the structure and properties of a representative molecular building block of formula [VO(TPP)] (TPP = tetraphenylporphyrinate) (**2**) have been compared with those of the 3D MOF **1**. Pulsed electron paramagnetic resonance measurements on magnetically diluted samples in titanyl isostructural analogues revealed that coherence times are retained almost unchanged for **1** with respect to **2** up to room temperature, while the temperature dependence of the spin-lattice relaxation time revealed insights on the role of low energy vibrations, detected through terahertz (THz) spectroscopy, on the spin dynamics.

INTRODUCTION

Quantum bits, or qubits, represent the elementary units for the realization of quantum computers[1] as well as the active units of potential quantum sensors.[2–4] For both applications, the quantum superposition of state that characterizes qubits physical realizations is exploited for specific purposes. In quantum computation, a highly coherent superposition state allows for the retention of the quantum information on the qubits for a time longer than that required to perform a quantum operation (quantum gate), whereas in quantum sensing a loss of coherent superposition is used to probe the presence of environmental perturbations. Nowadays, finding suitable, robust, and scalable systems as potential qubits represents one of the main challenges in chemistry, physics and materials science for the development of these technological applications.

Many physical systems, such as photon,[5] trapped ions,[6] quantum dots,[7] and coherent coupled systems of superconducting qubits[8] with nitrogen-vacancy centers in diamond[9–11] are

investigated as qubits candidates, each of them showing both merits and demerits. Among these qubits realizations, molecule-based spin qubits have been investigated only recently and have shown remarkable advantages, such as the capacity of facile addressing via pulsed electron paramagnetic resonance (EPR) techniques[12] - although not yet at the single qubit level - a high processability through surface deposition,[13] and a high degree of chemical tunability.[14,15] These features are crucial for their practical development and are not easily satisfied for other classes of potential qubits, such as, for example, electronic defects in extended inorganic solids.[9–11] On the other hand, molecular spin qubits often suffer from a relatively short lifetime of the quantum superposition states compared to other potential systems. This loss of information is related to the spin-spin relaxation time T_2, that is usually estimated by measuring the phase memory time T_m, which is a lower limit of T_2. Interactions with the environment contribute to the collapse of the already fragile superposition state of electronic spins in a process known as decoherence. In this respect, intense investigations aimed at increasing molecular qubits performance through chemical design have been reported in recent years.[16–22]

Another feature that places molecule-based spin qubits in a noteworthy position with respect to electronic defects in extended inorganic solids is the potential spatial control over qubit-qubit distances achievable through coordination chemistry approaches. Indeed, extended coordination polymers, or metal-organic frameworks (MOFs), with specific structural features such as overall dimensionality (bidimensional, 2D, or tridimensional, 3D), type of structural backbone (cubic, hexagonal), and controlled internal surface area, can be prepared at will through a wise selection of the molecular building blocks and well-developed coordination chemistry strategies.[23–25] This bottom-up approach can play a key role for quantum computation in increasing the scalability of the system by controlling the number of interconnected qubits within an extended network. This is equally relevant for quantum sensing, since extended porous networks allow analytes to diffuse selectively inside the voids of the solid and to be precisely detected by the qubit sensor units.[4,26–28]

The above mentioned bottom-up approach has been employed for the preparation of 2D nanosheets embedding Cu^{II}-tetracarboxyl-phenylporphyrinate units,[29] and a porous 3D network obtained linking Co^{II}-tetracarboxyl-phenylporphyrinate complexes through $[Zr_6(OH)_8]$ units.[30] For both materials the coherence times of the corresponding Cu^{II} and Co^{II}-based electronic spin qubits have been investigated. In the latter, the strong hyperfine-coupling induces a mixing of M_S and M_I levels of the $S = 1/2$ and $I = 7/2$ electronic and nuclear spin values of Co^{II}. This generates an avoided level crossing at low magnetic fields (< 0.3 T), whose related EPR transitions frequencies are characterized by a weak magnetic field dependence, *i.e.* $\Delta f/\Delta B = 0$.

Such a condition is typically observed for isolated atoms and can be used for the realization of a certain class of atomic clocks, thus these transitions assume the name of clock transitions. Such transitions are particularly insensitive to the magnetic noise, leading to enhanced coherence. However, it is exactly the low sensitivity to magnetic noise that makes them not ideal for quantum sensors applications, as also pointed out by the authors of the study.[30]

It should be also considered that room temperature coherence is highly desirable for sensing purposes. In this temperature regime, spin-lattice relaxation is a limiting factor. Indeed, both local and extended vibrational modes (phonons) can be significantly modified passing from isolated molecules that weakly interact in the crystal structure, mainly through non-covalent interactions, to extended molecular networks, where the units are covalently linked. This can induce relevant modification on the spin dynamics.[22,31–33]

For the design of molecular spin qubit with viable coherence times, oxidovanadium(IV) complexes constitute one of the most promising choice thanks to the weak orbital contribution to the magnetism and an inefficient spin-phonon coupling interaction, which provides long spin-lattice relaxation even at room temperature.[16,34] The characterization of the spin-lattice relaxation time, T_1, is then crucial in the design of highly performing molecular spin qubits since this process provides an upper limit for the coherence time.[13] Moreover, the investigation of spin-lattice and coherence times of vanadyl-based potential qubits embedded into a 3D crystalline material has not been reported yet.

Motivated by the need to acquire additional insights on the role of the crystal lattice properties in determining electronic spin qubits performance, here we report the preparation of a porous vanadyl-based 3D MOF of formula [VO(TCPP-Zn_2-bpy)] (**1**) (TCPP = tetracarboxyl-phenylporphyrinate; bpy = 4,4'-bipyridyl). The spin-lattice relaxation times of **1** were studied by alternate current (AC) susceptibility measurements, and the coherence times of an isostructural magnetically diluted sample [$VO_{0.05}TiO_{0.95}$(TCPP-Zn_2-bpy)] (**1'**) were investigated through pulsed-EPR spectroscopy. The results have been compared to those obtained on a representative mononuclear molecular building block (0D) of formula [VO(TPP)] (TPP = tetraphenylporphyrinate) (**2**) and its isostructural magnetically diluted sample [$VO_{0.02}TiO_{0.98}$(TCPP)] (**2'**). The analysis of the temperature dependence of the spin-lattice relaxation time, which plays a crucial role in determining the coherence at room temperature for the two materials, is discussed considering the different structural and spectroscopic features in the terahertz regime shown by the 3D network and the 0D mononuclear analogue.

RESULTS

Design & Synthesis. Metalated tetraphenylporphyrins have been largely employed as molecular building blocks for the preparation of regular 3D hetero- and homo-metallic MOFs.[30,35,36] Unlike other metalloligands, their planar and symmetric structure is ideal to both accommodate a large variety of metal ions inside the porphyrinate macrocycle, or to prepare crystal structures with well-defined topologies. In particular, it has been shown that combination of metalated tetracarboxyl-phenylporphyrinates with bare divalent metal ions such as Zn^{II} or Cu^{II}, and a pillar-like molecular ligand such as bpy, allows preparation of porphyrinate paddle-wheel frameworks for which the 3D stacking is controlled by the coordination geometry of the porphyrin metal center (Figure 1).[35]

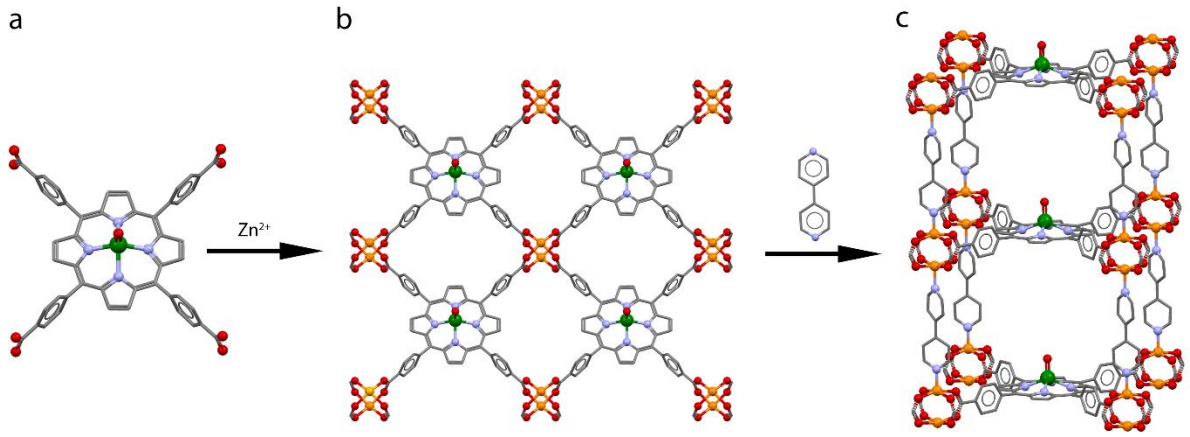

Figure 1. Schematic representation of the two-step self-assembling process responsible for the formation of the 3D MOFs **1** and **1'**. Color codes: green: vanadium, orange: zinc, red: oxygen, light blue: nitrogen, gray: carbon. Hydrogen atoms are omitted for graphical clarity.

As an example, tetracoordinated ions such as Mn^{II} and Fe^{II} ions easily allow further axial coordination with the N-donating pillar ligand, while Pt^{II} and Ni^{II} prefer to maintain the square planar coordination geometry of the porphyrin macrocycle; in the latter case, further axial coordination is limited to the bridged Cu^{II} and Zn^{II} ions within the paddle-wheel motif.[35] The case of oxidovanadium(IV) is expected to be peculiar because further coordination with the pillar-like ligand is in this case hampered by the preformed bond between V^{IV} and the oxido ligand, which results in an overall modification of the coordination geometry of the metal center to a square pyramidal one.

Within this general scheme, the reaction between preformed vanadyl- and/or titanyl-tetracarboxyl-phenylporphyrinates with Zn^{2+} and bpy has been performed to obtain the 3D structure reported in Figure 1c.

The synthesis of the vanadyl tetracarboxyl-phenylporphyrinate [VO(TCPP)] building block has been achieved by following a reported procedure that has been adapted to the oxidovanadium(IV) ion.[37] It consists in the reaction between the vanadyl precursor [$VO(acac)_2$] ($acac^-$ = acetylacetonate) and the tetrakis(4-carboxyphenyl)porphyrin ligand with carboxyl groups protected by ester functionalities, H_2TMeCPP (tetrakis(4-methoxycarbonylphenyl)porphyrin), in PhOH at reflux temperature (Scheme 1a).

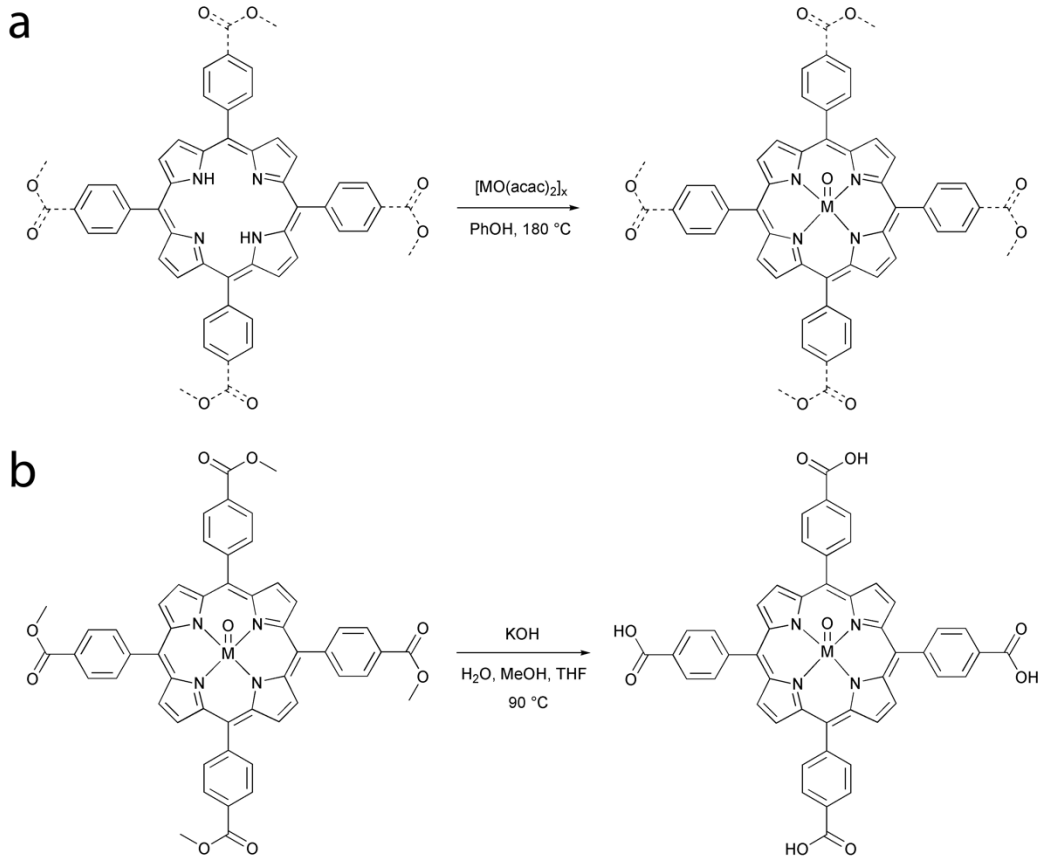

Scheme 1. Reaction schemes for the synthesis of vanadyl and titanyl tetraphenylporphyrin derivatives (M = V, Ti; x = 1, 2).

Subsequent deprotection of the ester groups through basic hydrolysis provides the [VO(TCPP)] molecular building block (Scheme 1b). The same reaction conditions have been used to prepare the 0D reference compound [VO(TPP)] (**2**) as well as the titanyl diamagnetic analogues [TiO(TCPP)] and [TiO(TPP)] (**3**) (Scheme 1). It should be highlighted that metalation of the tetracarboxyl-phenylporphyrin with the oxidovanadium(IV) moiety is easily accomplished within ca. 6 hours of reaction, whereas metalation with the oxidotitanium(IV) ion appears to be more difficult, requiring longer reaction times (ca. 36 hours) and a larger excess of the titanyl precursor [$TiO(acac)_2]_2$. This chemical inertness is reflected by the lack of titanyl

porphyrinates reported so far in the literature with respect to other transition metal ion derivatives, including the vanadyl analogues.

Self-assembly of vanadyl tetracarboxyl-phenylporphyrinate building blocks, Zn^{2+} and bpy in DMF at 80 °C followed by slow cooling to room temperature provides air-stable red cubic single crystals of compound **1** suitable for X-ray diffraction analysis. The magnetically diluted sample **1'** was prepared by following the same synthetic procedure developed for the preparation of **1** by reacting a mixture of [VO(TCPP)] and [TiO(TCPP)] in 5:95 molar ratios with Zn^{2+} and bpy. Instead, the magnetically diluted samples **2'** and **2''** were prepared by recrystallization of [VO(TPP)] and [TiO(TPP)] in 2:98 and 30:70 molar ratios, respectively. The difference in the nominal concentration of paramagnetic species between the two lower concentrated materials has been designed to achieve similar spin concentrations in view of the presence of large voids for the 3D compound **1** with respect to the 0D compound **2** (*vide infra*).

Crystal Structures. Compound **1** crystallizes in the tetragonal *P4* space group with one anionic complex, two Zn^{2+} ions and one bpy molecule in the unit cell, the asymmetric unit being one fourth of the molecule. The peripheral carboxyl substituents of the porphyrin macrocycle (Figure 1a) interact with Zn^{2+} to form 2D layers where the porphyrin units are connected in a four-folded symmetry through $[Zn_2(COO)_4]$ subunits (Figure 1b), similarly to what recently reported for $[Cu(TCPP)\text{-}Zn_2(H_2O)_2]$.[29] The pillar-like ligands bpy then allow connection between the 2D layers to form a 3D MOF by further axial coordination between pairs of $[Zn_2(COO)_4]$ subunits (Figure 1c). The obtained structure has 3D channels with a pore dimension of 1.66 × 1.38 nm^2 along the *a* and *b* axes. The percentage of void volume in the structure of **1** was estimated to be ca. 74 % (2842 $Å^3$) and 72.8 % (2795 $Å^3$) of the total volume (3838 $Å^3$) considering H_2 and N_2 as probe gases, respectively (kinetic radii, H_2, r = 1.40 Å; N_2, r = 1.82 Å).[38]

The coordination geometry of the Zn^{2+} ions, which templates the formation of the overall crystal structure, consists in a square pyramid where pairs of Zn^{2+} ions are bridged in a μ-type binding mode by four carboxylate ligands. The resulting equatorial plane around each Zn^{2+} ion is thus formed by four oxygen donor atoms, while the axial position of the square pyramid is completed by the nitrogen donor of a bpy ligand, which bridges pairs of Zn^{2+} ions from adjacent 2D layers (Figure 2a).

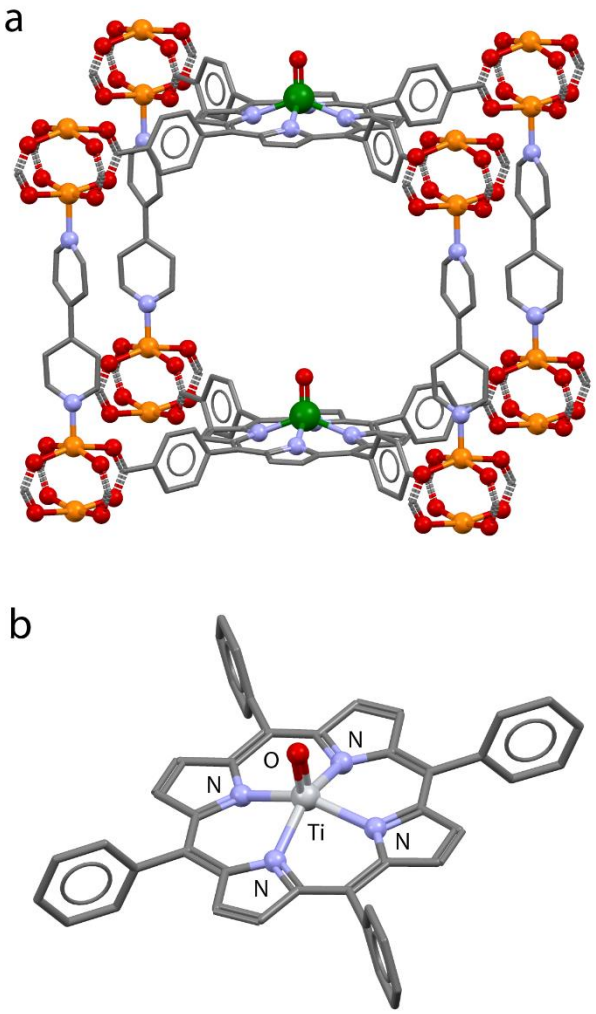

Figure 2. Molecular structures of compounds **1** (a) and **3** (b) with coordination geometry of the metal ions highlighted. Color codes: green: vanadium, orange: zinc, silver: titanium, red: oxygen, light blue: nitrogen, gray: carbon. Hydrogen atoms and disordered fragments are omitted for graphical clarity.

The molecular structure of the anionic complex $[VO(TCPP)]^{4-}$ shows a vanadium(IV) ion in a square pyramidal coordination geometry with the metal ion slightly above the basal plane (ca. 0.59 Å) formed by the four nitrogen donor atoms of the porphyrin macrocycle (Figure 2a). The V=O moiety is sitting on the four-fold symmetry axis and is disordered on two positions, symmetric with respect to the macrocycle ring, with 50:50 occupancy factors, leading to a non-polar crystal structure. The V–O and V–N distances, 1.60 Å and 2.09 Å respectively, are in agreement with what is usually encountered for similar vanadyl complexes. The planes of the phenyl substituents are 90° tilted with respect to the plane of the porphyrin macrocycle, in agreement with what observed for analogous MOFs based on isostructural building blocks (Figure 2a). This leads to an overall crystal structure of tetragonal symmetry where all vanadyl

moieties are oriented along the *c* axis (Figure S1). The V···V shortest distances in the crystal structure of **1** correspond to the unit cell distances, *i.e.* 13.9 Å along the *c* axis and 16.6 Å in the *ab* plane. Finally, it should be noted that the pyridine rings of the bpy ligand appear disordered in two 90°-tilted orientations, with the orientation of the two independent rings 45°-tilted with respect to each other.

Single crystals suitable for X-ray diffraction analysis of compounds **2** and **3** were obtained by slow evaporation of CH_2Cl_2 solutions. Both compounds crystallize in the tetragonal *I4* space group with two neutral complexes in the unit cell; even in this case the asymmetric unit is one fourth of the molecule. Due to the better quality of the collected diffraction data and the isostructurality between the two compounds, here we report only the data related to the [TiO(TPP)] compound **3**.

The crystal structure of **3** consists of neutral titanyl tetraphenylporphyrinate complexes with all Ti=O units lying on the fourfold symmetry *c* axis (Figure S2). The shortest M···M distance is 10.9 Å and involves metal complexes of adjacent layers. No significant intermolecular contacts involving the phenyl rings are present. The molecular structure of the complex is reported in Figure 2b. The coordination geometry around the Ti^{IV} ion is a square pyramid with a Ti–O distance of 1.58 Å and Ti–N distances of 2.11 Å. As already observed for **1**, the metal-oxido cationic moiety is disordered along the tetragonal axis on two positions with equal occupancy factors, with the metal center lying 0.58 Å from the basal plane of the porphyrin macrocycle.

Powder X-ray diffraction (PXRD) patterns were recorded on polycrystalline samples of all investigated systems, both pure compounds and crystalline dispersions, to ascertain their structural phase homogeneity. This is clearly evidenced by the good agreement between experimental and simulated patterns (Figures S3–S4).

Magnetization dynamics. AC susceptibility measurements were performed on microcrystalline samples of compounds **1**, **2** and the crystalline dispersion **2''** to investigate their magnetization dynamics. The choice to study the dilution **2''** is due to the pronounced difference in the spin concentration between **1** and **2**. Indeed, the spin concentration for **1** is 0.26 spin nm^{-3}, whereas for **2** it is 1.1 spin nm^{-3}. **2''** provides a spin concentration of 0.34 spin nm^{-3}, which is closer to that of **1**, and thus associated to a comparable dipolar internal magnetic field.

As commonly observed for $S = ½$ molecular spin qubit systems, the thermal variation of the complex magnetic susceptibility in zero static magnetic field reveals no out-of-phase

component of the susceptibility (χ'') in the whole investigated temperature range. When a small static magnetic field (> 40 mT) is applied, slow magnetic relaxation is observed for all samples with appearance of a peak in the out-of-phase component of the susceptibility and a concomitant decrease of the in-phase part (χ') (Figures S5-S17).[13,34] The relaxation time, τ, which is representative of the spin-lattice relaxation, was obtained by simultaneously fitting the real and imaginary components of the magnetic susceptibility with the generalized Debye model (see Supporting Information).[39] The extracted values of τ for **1**, **2** and **2''** obtained under a static magnetic field B = 1.0 T scanning the temperature, are reported in Figure 3a in a log(τ) vs log(T) plot.

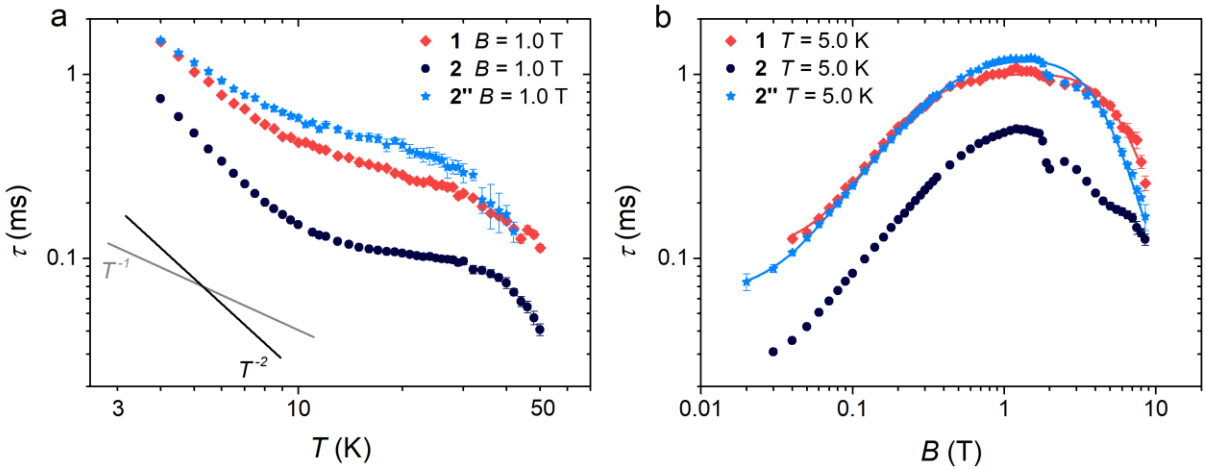

Figure 3. Temperature (a) and magnetic field (b) dependence of τ extracted from AC susceptibility measurements for microcrystalline samples of compounds **1**, **2** and **2''** under an applied static magnetic field of 1.0 T (a) and in the 0.0–8.5 T range at 5.0 K (b). Solid lines are the best-fit of the models (see text).

The absolute values of the spin-lattice relaxation times are comparable for **1** and **2''** in a wide temperature region, whereas those of **2** are lower, thus following the trend of the spin concentrations. The temperature dependence of τ shows a qualitatively similar behavior for the three compounds in the entire T range. At the lowest temperatures, between 4 and 10 K, the spin-lattice relaxation time shows a T^{-2} dependence, which suggests the presence of an important spin-phonon bottleneck effect.[40,41] This phenomenon affects the direct spin-lattice relaxation mechanism in magnetically concentrated samples and is particularly relevant in vanadyl-based molecules.[42] Figure 3a shows that in the 10–30 K range, an unexpected remarkably weak temperature dependence of τ is observed, with an exponent significantly lower than the unity expected for a pure direct mechanism relaxation process.[43] For T > 30 K, τ of both compounds exhibits a faster decrease with increasing temperature.

To have a better understanding of the relaxation mechanisms involved in such compounds, the magnetization dynamics was also studied as a function of the static magnetic field in a wide magnetic field range (0.0−8.5 T) at different temperatures (5.0 K, 7.5 K and 10.0 K) for each compound (Figures S9−S17). The relaxation times extracted with the generalized Debye model at 5.0 K are shown in Figure 3b, while the data obtained at all investigated temperatures are reported in Figures S18−S20. All compounds show the expected non-monotonous behavior of the relaxation time, with an increase of τ at low field, a plateau at intermediate fields, and then a decrease at high fields. In the low field region, up to 1.0 T, spin-spin and spin-nuclei interactions, which promote spin relaxation by breaking the time-reversal symmetry of the Kramers doublet,[44,45] are suppressed by the increasing of the magnetic field, resulting in a rapid growth of τ. Instead, in the high field region, beyond 3.0 T, the strong field dependence of the direct mechanism causes the rapid decrease of τ. Indeed, the larger is the Zeeman splitting of the two M_s states, the larger is the number of phonons matching this energy difference.

The absolute values of the relaxation times of **1** and **2''**, as well as the magnetic field dependence, are again comparable, whereas **2** shows lower values of τ, in agreement with its temperature dependence (Figure 3a). A striking feature in the magnetic field dependence of the relaxation times is the dip shown by all compounds at 2.0 T. This feature is particularly pronounced for **2** (Figure S21) and less pronounced for **2''**, suggesting that the presence of this dip might be related to the spin-phonon bottleneck effect. However, the reason why an acceleration of the relaxation rate at 2.0 T is observed, is, at the moment, unclear. To check if an anomalous temperature dependence of τ is also present at this field value, AC susceptibility data for compound **2** were recorded also at 2.0 T, showing a very similar behavior (Figure S22).

The magnetic field dependence of τ for **1** is reproduced by the Brons – van Vleck model[45,46] with a slight modification (eq. 1):

$$\tau^{-1} = d\left(\frac{1 + eB^2}{1 + fB^2}\right) + cB^m \qquad (1)$$

The first term is related to the low-field region where τ increases due to the suppression of the internal fields, whereas the second term accounts for the direct relaxation mechanism. In the standard Brons – van Vleck model, the direct contribution to the spin-lattice relaxation rate in Kramers systems depends on the field as $\tau^{-1} \propto cB^4$. This has indeed been confirmed by previous

studies on vanadium-based molecular spin qubits.[13,16,22,32,34,42] However, in this case τ shows a weaker magnetic field dependence, and the best-fits of the experimental data obtained for **1** assuming different integer values of *m* (Figures S23–S25 and Table S1) clearly favor a cubic field dependence. This points to a non-conventional direct relaxation mechanism, in agreement with the observed anomalous weak temperature dependence of τ.

The extended Brons-van Vleck model[32] has been used to properly reproduce the data obtained for **2''**:

$$\tau^{-1} = d\left(\frac{1+eB^2}{1+fB^2}\right) + g\left(\frac{1+eB^2}{1+hB^2}\right) + cB^m \qquad (2)$$

In this case, a second term accounting for the suppression of the internal fields due to the increase of the magnetic field is introduced. The use of the extended law is justified in Figure S26, where the data of **2''** are fitted with both models, while Table S1 contains the best-fit parameters for the three different temperatures. Finally, it should be highlighted that the modelling of the magnetic field dependence of the spin-lattice relaxation time for **2** is not feasible because the distortions observed between 2.0 and 7.0 T do not allow for reasonable fits with both standard and extended Brons – van Vleck models.

Continuous Wave and Pulsed Electron Paramagnetic Resonance Spectroscopy. While AC susceptometry provides useful information about spin-lattice relaxation as a function of the applied static magnetic field in concentrated samples, pulsed EPR spectroscopy allows to determine both spin-lattice and spin coherence relaxation times for magnetically diluted systems in a wide temperature range.

Continuous wave (CW) and echo-detected field-swept (EDFS) EPR spectra of the diluted compounds **1'** and **2'** recorded at T = 10 K and T = 50 K, respectively, are reported in Figure 4 together with their simulations.

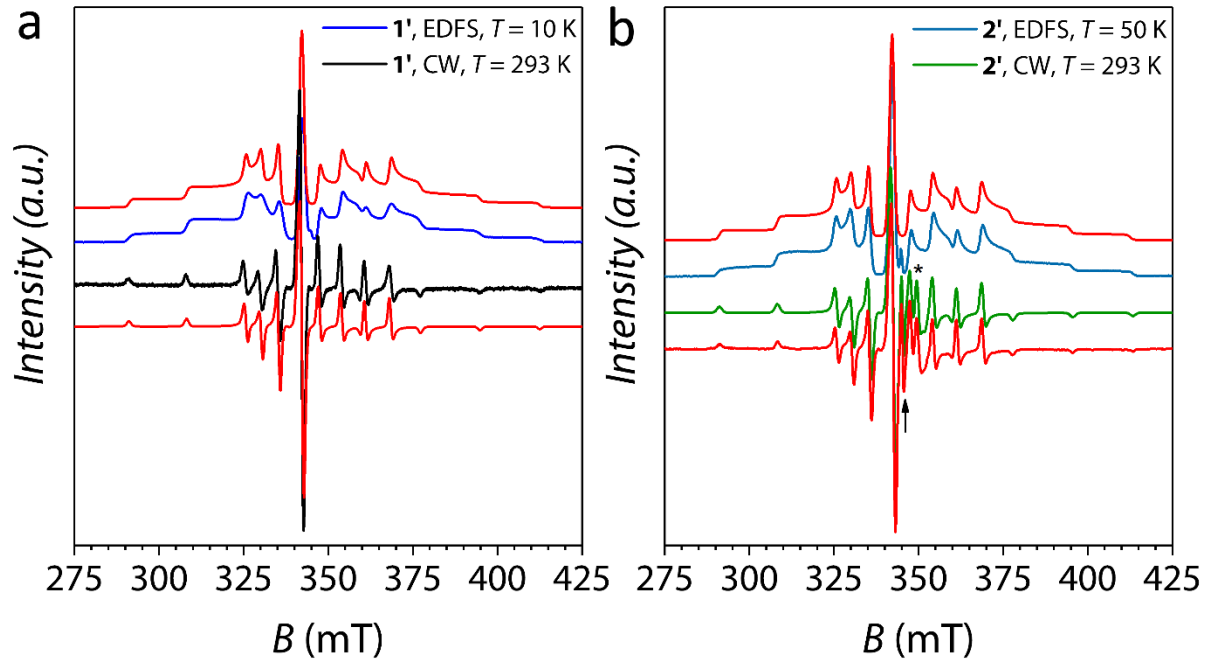

Figure 4. Experimental and simulated CW and EDFS EPR spectra for **1'** (a) and **2'** (b) at X-band frequency (9.7 GHz). Spectral simulations corresponding to the spin Hamiltonian parameters reported in Table 1 are shown in red. The asterisk and the arrow on the CW EPR spectrum of **2'** evidence the presence of unavoidable paramagnetic impurities that have been included in the simulation (see text and Supporting Information for further details).

Both compounds show similar spectra that are characterized by the eight-fold hyperfine structure due to the coupling between the $S = 1/2$ electronic spin of V^{IV} and the $I = 7/2$ nuclear spin of its most abundant isotope (^{51}V, abundance 99.76%). The signals are further split by the anisotropic components of the hyperfine coupling in perpendicular and parallel directions. Spectral simulations[47] were then performed using the following spin Hamiltonian

$$\mathcal{H} = \hat{\boldsymbol{I}} \cdot \boldsymbol{A} \cdot \hat{\boldsymbol{S}} + \mu_B \hat{\boldsymbol{S}} \cdot \boldsymbol{g} \cdot \boldsymbol{B} \qquad (3)$$

to evaluate the anisotropy of the $\boldsymbol{g}$ factor as well as of the hyperfine coupling constant $\boldsymbol{A}$. The experimental spectra can be satisfactorily reproduced assuming an axial model (*i.e.* x = y ≠ z) for both compounds, in agreement with the tetragonal site symmetry of the molecular systems. The best-fit parameters are reported in Table 1.

Table 1. Best-fit parameters extracted from simulation of the experimental spectra of **1'** and **2'**.

Compound	g_x	g_y	g_z	$\lvert A_x \rvert$ (MHz)	$\lvert A_y \rvert$ (MHz)	$\lvert A_z \rvert$ (MHz)
1'	1.9865(1)	1.9865(1)	1.963(1)	168(2)	168(2)	477(2)
2'	1.9865(1)	1.9865(1)	1.963(1)	169(2)	169(2)	480(2)

The parameters reported in Table 1 agree with those expected for vanadyl porphyrinate derivatives[48,49] and correspond to a ground state with the unpaired electron in a d_{xy} orbital. It is evident that the EPR spectrum of **2'** also shows some weak features (< 4% of the total signal and indicated in Figure 4b) which cannot be attributed to vanadyl species. On the basis of the best simulation parameters (Figure S27 and Table S2) these were attributed to radical monoanionic ligand and a residual Ti^{III} species.

Hyperfine Sublevel Correlation (HYSCORE) experiments have been performed on the two compounds to detect and determine the hyperfine interactions due to the ligand nitrogen atoms of the porphyrin ring and nearby hydrogens. The spectra of **1'** and **2'** (Figures S28–S29) are practically superimposable and typical for vanadyl porphyrin and phthalocyanine molecular systems.[49] Spectra simulation (Figure S30) provided ^{14}N hyperfine and quadrupole splitting parameters that well compare with previously reported data on similar coordination environments (Table S3).

The intense spin-echo detected EPR spectrum let us anticipate that quantum coherence could be measured for both compounds. Moreover, the spin Hamiltonian parameters obtained through the simulation of the CW spectrum provide good simulations of the EDFS spectra as well, hence indicating that the entire paramagnetic components are experiencing the detected coherence.

Inversion recovery experiments on **1'** and **2'** were performed in the 5.0–290 K temperature range at X-band frequency to investigate the temperature dependence of the spin-lattice relaxation time T_1 at the resonant magnetic field corresponding to the hyperfine transition $M_I = -1/2 \rightarrow +1/2$. The resulting saturation recovery traces were fitted with a stretched-exponential equation

$$I = I_0 + k_1 exp\left[-\left(\frac{\tau_p}{T_1}\right)^{\beta_1}\right] \qquad (4)$$

and the extracted T_1 values (Tables S4–S5) as a function of T are reported in Figure 5.

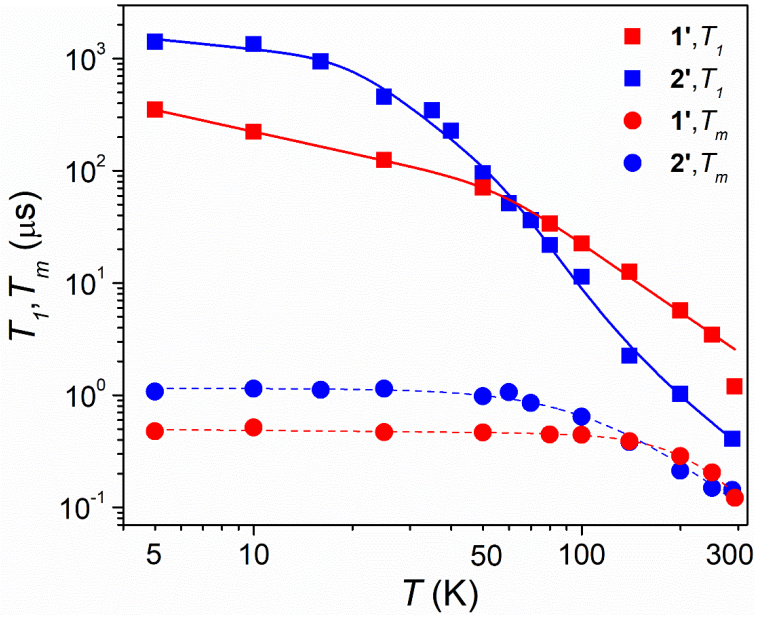

Figure 5. Temperature dependence of T_1 and T_m for **1'** and **2'** (see legend) from pulsed EPR inversion recovery experiments at X-band frequency. Solid lines are the best-fits considering local vibrational modes according to eq. (7). Short-dashed lines represent a guide for the eyes. Error bars are within the size of the symbols.

The temperature dependence of T_1 for the magnetically diluted samples **1'** and **2'** shows an increase of the slope on rising the temperature, which is characteristic of the crossover from a dominating direct process of relaxation at low temperature to a Raman mechanism at high temperatures. T_1 values of **1'** at low temperature are ca. one order of magnitude lower than that of **2'** despite the similar spin concentration of the two compounds. As the temperature increases, the spin-lattice relaxation time for **2'** starts to decrease more abruptly above 30 K, whereas **1'** shows such a behavior only at higher temperature and with a weaker temperature dependence. Consequently, the curves for the two compounds intersect around 60 K, and at room temperature T_1 for **1'** reaches a value of ca. 1 μs vs 0.6 μs observed for **2**.

Different analytical functions are commonly used to reproduce the temperature dependence of T_1.[50] Here, the experimental data are well reproduced (Figure S31) by the phenomenological relation

$$T_1^{-1} = a_{dir}T^x + a_{Ram}T^n \qquad (5)$$

where, unlike to previous reports, the exponent x of the temperature dependence of the direct process is left free to vary from the unitary value which is expected for the direct process.[43] The best-fit values for the direct process are x = 0.54(6) and x = 0.3(3) for **1'** and **2'**, thus deviating

significantly from unity. On the other hand, the Raman process exponents, n = 2.5(1) and 3.4(1) for **1'** and **2'** respectively, are within the usual range observed for vanadyl complexes (n ca. 3).[13,16,34,51] It is worth noting that replacement of the second term of eq. (5) with the Debye transport integral function (equation S3) does not significantly improve the overall fitting of data for **1** and worsen that for **2** (Figure S31 and Table S6).

To investigate the quantum coherence in detail and to determine the phase memory time, T_m, for **1'** and **2'** as a function of the temperature, echo decay experiments were also performed. Because T_1 values, which limit the T_m values especially at high temperatures, are sufficiently long for both compounds in the whole investigated temperature range, echo decay traces were detected up to room temperature for both **1'** and **2'**. The decay traces were fitted using the stretched-exponential equation

$$I = I_0 + k_m exp\left[-\left(\frac{2\tau_p}{T_m}\right)^{\beta m}\right] \qquad (6)$$

as usually done for transition metal systems,[50] where I indicates the echo intensity, $2\tau_p$ is the delay between the initial pulse and the echo detection and β_m is the stretch factor. The temperature dependences of T_m for **1'** and **2'** are reported in Figure 5.

The thermal variation of T_m for **1'** and **2'** shows an almost temperature independent behavior in the 5.0–100 K range for **1'** (ca. 0.5 μs) and in the 5.0–60 K range for **2'** (ca. 1.0 μs), with relative values that follow the corresponding T_1 ones. These values are comparable to those recently reported for a 2D network formulated as [Cu(TCPP)-$Zn_2(H_2O)_2$] and the relative mononuclear building block [Cu(TPP)] measured in a frozen solution, although coherence times data are only available up to 90 K.[29] At 150 K, T_m assumes the same value for **1'** and **2'** (ca. 0.4 μs) and decreases to reach the lowest values at room temperature (ca. 0.14 μs). It is interesting to note that a crossover between the T_m values of **1'** and **2'** occurs in much the same way as observed for T_1 at slightly lower temperatures.

To prove that the observed coherence times for **1** and **2'** allow to perform coherent spin manipulations, *i.e.* to place the spins in any arbitrary superposition of states, nutation experiments were performed at different microwave powers. Remarkably, Rabi oscillations were clearly observed with the expected linear dependence of the Rabi frequency, Ω_R, as a function of the microwave attenuation for both **1'** (Figure 6) and **2'** (Figure S32).

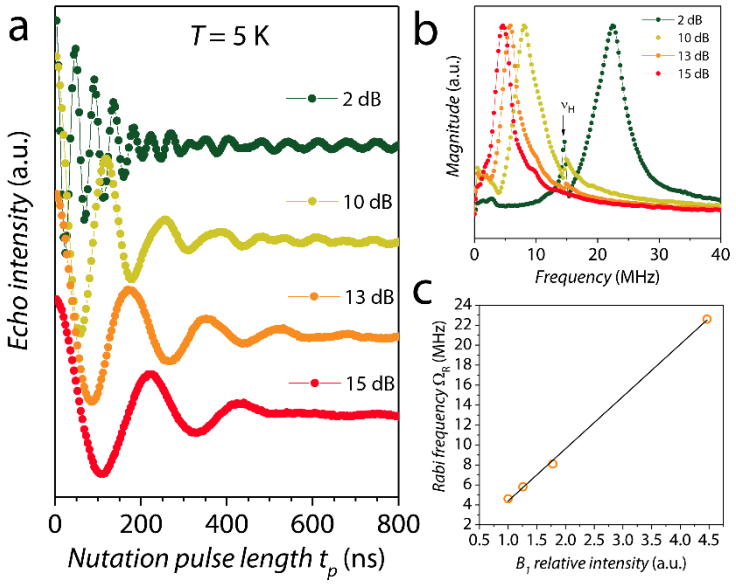

Figure 6. (a) Rabi oscillations recorded for **1'** at 5 K for different microwave attenuations (X-band). (b) Fourier Transform of the Rabi oscillations. (c) Linear dependence of the Rabi frequency (Ω_R) as a function of the relative intensity of the oscillating field B_1.

THz Vibrational Spectroscopy. Terahertz spectra, corresponding to the 10–110 cm^{-1} range, were recorded by time-domain transmission spectroscopy (THz-TD) on polycrystalline samples of **1** and **2** dispersed in polyethylene pellets.

A striking difference between the isolated [VO(TPP)] units of **2** and the extended structures of **1** is observed. Indeed, **2** shows a well-defined absorption band at ca. 67 cm^{-1}, which is absent in **1** (Figure 7).

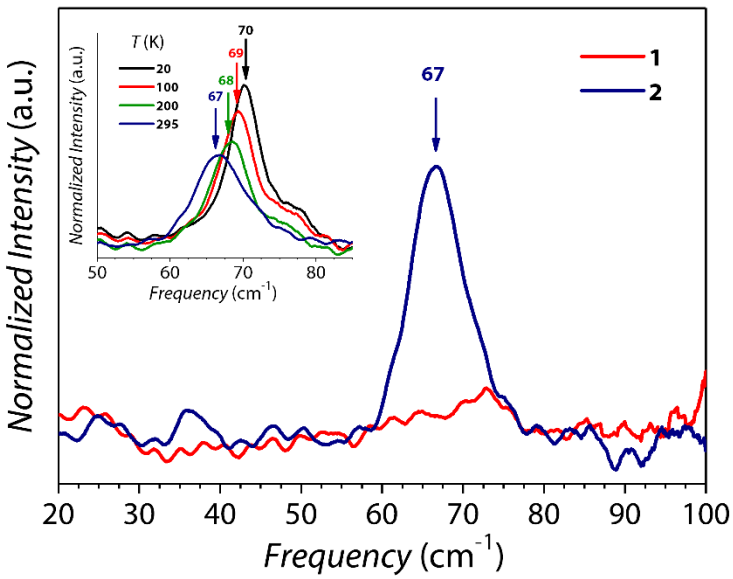

Figure 7. Vibrational spectra in the 0.6–3.0 THz range (20–100 cm^{-1}) of compounds **1** and **2** recorded at 295 K. The arrow indicates the frequency of the absorption. Inset shows the temperature dependence (20–295 K range) of the absorption spectra of **2**.

Assignment of the low energy absorption of **2** is not straightforward because porphyrinate complexes show metal-ligand vibrations that are often mixed with porphyrin ring deformations.[52–54] Moreover, previous theoretical studies on simpler vanadyl-based potential molecular qubits showed that in the THz frequency range a strong admixing between local and collective degrees of freedom is also present.[32]

The temperature dependence of the spectra of **2** (inset in Figure 7) shows a pronounced narrowing and shift to higher frequency of the absorption peak on lowering the temperature. According to the idea that structure stiffening at low temperature is expected to increase the vibration energy of collective modes, we can deduce that a significant contribution of collective vibrations to the nature of this mode is present. This is also in agreement with the lack of this mode in the covalent lattice of **1**, as well as its similar frequency in the titanyl derivative **3** (Figure S33).

DISCUSSION

Our investigation proves the successful inclusion of paramagnetic vanadyl units in a well structurally characterized MOF, which is, to the best of our knowledge, unprecedented though not unexpected. More relevant is the preservation of spin coherence at room temperature, with comparable coherence times for the MOF and the mononuclear unit. This is a remarkable result because it allows to apply pulsed EPR techniques, which are known to provide more detailed information on the nature and the adsorption mode of guest molecules than CW techniques.[55,56]

The origin of this appealing behavior can be rationalized thanks to the comparative study that we have performed. First of all, it is important to stress that the electronic structure of the vanadyl unit is practically identical in the MOF and in the isolated molecule. This is clearly demonstrated by the very minor modifications of the Spin Hamiltonian parameters, reported in Table 1, as well as of the hyperfine coupling values with neighboring nuclei detected by HYSCORE and listed in Table S3. It is also interesting to note that some characteristic features of the spin dynamics are preserved on increasing the material dimensionality, such as the field dependence of the magnetization relaxation time that shows a wide plateau extended up to

several Tesla as reported in Figure 3b. This behavior, typical of the V^{IV} ion and much more pronounced than in analogous S = 1/2 systems based, for example, on Cu^{II},[29] allows high-field/high-frequency applications without significant acceleration of the spin dynamics.

Another common feature between the MOF and isolated molecule is the very weak temperature dependence of the spin-lattice relaxation time in the temperature range 10–30 K, where magnetic relaxation is dominated by the direct mechanism and a linear dependence with temperature is expected. Such a behavior was also observed, though not highlighted, for a vanadyl-phthalocyaninate complex.[34] As data for the latter were collected on less concentrated samples with respect to those investigated here, we can safely exclude that an intermolecular processes of relaxation is responsible for such a phenomenon. This leads us to associate this peculiarity to the macrocyclic coordination mode, although a rational for it is still lacking.

In contrast to this remarkable similarity, **1** and **2** differ significantly in their low energy vibrational spectrum. The first IR active vibrational mode, occurring at 67 cm^{-1} for **2**, exceeds our accessible range (110 cm^{-1}) in **1**. This originates remarkable differences in the temperature dependence of T_1 above 30 K. Local vibration modes have already been considered as sources of magnetic relaxation, but the support of optical investigations is uncommon.[57,58] We have therefore reproduced the temperature dependence of the spin-lattice dynamics through the already proposed phenomenological model[50]

$$T_1^{-1} = a_{dir}T^x + a_{loc}\frac{\exp(\hbar\omega/k_BT)}{(\exp(\hbar\omega/k_BT)-1)^2} \qquad (7)$$

where ω is the frequency of the vibrational mode and a_{dir} and a_{loc} are coupling coefficients as in equation (5). The T_1 data of **1** are successfully simulated (Figure 5) with x = 0.64 and ω = 184(2) cm^{-1}, thus suggesting that the first active mode is present at a frequency higher than our accessible spectral range. Data simulation of **2** were performed by fixing the frequency of the vibration mode to 67 cm^{-1}, accordingly to spectral findings. The whole temperature range is well reproduced including a second mode at higher frequency, 303(35) cm^{-1}, to the model. This is not surprising because an increasing number of active vibrational modes is expected to be present at higher frequencies. Notably, similar unusually low x exponents of the direct process are obtained independently of the model used to simulate the data (see Table S6), confirming the robustness of the analysis.

CONCLUSIONS

In conclusion, we have successfully synthesized a 3D porous network embedding vanadyl spin units that retains spin coherence up to room temperature. This is a remarkable result for coherent magnetic sensing of potentially adsorbed species. Engineering of MOF structures with embedded vanadyl moieties acting as quantum spin sensors towards specific analytes seems indeed quite straightforward.

Our multitechnique investigation has also provided precious hints for a better understanding of the spin dynamics in molecular systems. In contrast to what could be intuitively expected, the inclusion of [VO(TPP)] units in an extended network does not affect the low temperature regime. The $n < 1$ exponent in the $T_1 \propto T^{-n}$ law seems rather typical of the rigidity of the tetraphenyl-porphyrin coordination environment. On the contrary, linking the vanadyl units in the 3D network has pronounced effects on the infrared active low energy vibrational modes. This reflects on the temperature dependence of T_1 in the intermediate temperature regime. The observed behavior is of paramount importance for quantum sensing as it warrants that spin coherence is not limited at room temperature by a rapid spin-lattice magnetic relaxation.

It also emerges from this study that the optimization of metal-organic frameworks performance through chemical design requires a deeper understanding of the role of intramolecular and intermolecular vibration in the spin dynamics. The first steps we can envisage in this direction is obtaining high quality IR spectra on a continuous range to detect the lowest vibrational mode of **1**. Recording also Raman spectra in the THz regime is also important as it will allow to exclude the presence of relevant low energy vibrational modes that might have remained undetected in the IR absorption spectra. The disorder in V=O orientation in fact symmetrizes the otherwise acentric crystal structures of **1** and **2**. Theoretical analysis of the vibrational modes and their coupling to the spin system would also add significant information, although they are expected to be particularly challenging for **1**. Finally, the results presented here highlight the potentiality of V^{IV} molecular units as highly coherent spin qubits units for quantum sensing applications despite a complex and nuclear spin-active rich crystal structure. This opens the doors for further studies focused on the spin coherence measurements in the presence of guest solvents inside the MOFs cavities, to probe its potential use as a molecule-based quantum sensor.

EXPERIMENTAL SECTION

General Remarks. All chemicals were purchased and used without further purification except for the tetrakis(4-methoxycarbonylphenyl)porphyrin (H_2TMeCPP), the precursor of tetrakis(4-carboxyphenyl)porphyrin (H_2TCPP), that was synthesized according to a previously reported study.[37]

Synthesis of [VO(TCPP)]·MeOH·2H_2O. H_2TMeCPP (1.00 g, 1.18 mmol) and [VO(acac)$_2$] (0.31 g, 1.18 mmol) were reacted at 180 °C in 5 mL of PhOH for 6 h. After that, the solvent was removed under vacuum and the resulting solid of [VO(TMeCPP)] was washed with EtOH and dried under vacuum. (Yield: 83%). [VO(TMeCPP)] (1.00 g, 1.10 mmol) was stirred in a mixture of THF (25 mL) and MeOH (25 mL). To this solution, a solution of KOH (2.65 g, 47.2 mmol) in H_2O (25 mL) was added. The mixture was refluxed for 12 h. After refluxing, THF and MeOH were removed under reduced pressure through rotary evaporation. Additional water was added to the solution, then the solution was acidified with 1 M HCl until no further precipitation occurred. The solid was collected by filtration, washed with water and dried in vacuum. Needle-shape crystals of [VO(TCPP)]·MeOH·2H_2O were obtained by slow evaporation (one week) of a MeOH solution of the crude [VO(TCPP)]. Yield: 95%. Elemental anal. calcd for $C_{49}H_{36}N_4O_{12}V$: C, 63.71; H, 3.93; N, 6.07; found: C, 64.04; H, 3.89; N, 6.11. FT-IR ($\tilde{\upsilon}_{max}$/cm^{-1}, KBr pellet): 3445m, 1696vs, 1606s, 1510vw, 1404m, 1276m, 1100w, 1005m, 803m.

Synthesis of [TiO(TCPP)]·H_2O. [TiO(TCPP)] was synthesized by following a slightly modified procedure with respect that of [VO(TCPP)]. H_2TMeCPP (260 mg, 0.31 mmol) and [TiO(acac)$_2$]$_2$ (97 mg, 0.37 mmol) were reacted at 180 °C in 5 mL of PhOH for 63 h. After that, PhOH was removed under vacuum. The resulting solid was dissolved into a mixture of THF (15 mL) and MeOH (15 mL). To this solution, a solution of KOH (0.7 g, 12.4 mmol) in H_2O (15 mL) was added. The mixture was refluxed for 12 h. After refluxing, THF and MeOH were removed under reduced pressure through rotary evaporation. Additional water was added to the solution, then the solution was acidified with 1 M HCl until no further precipitation occurred. The solid was collected by filtration, washed with water and dried in vacuum. Yield: 45 %. Elemental anal. calcd for $C_{48}H_{30}N_4O_{10}Ti$: C, 66.22; H, 3.47; N, 6.44; found: C, 66.79; H, 3.66; N, 7.03. FT-IR ($\tilde{\upsilon}_{max}$/cm^{-1}, KBr pellet): 2953m, 1692vs, 1603s, 1563vw, 1488vw, 1406w, 1248m, 1106w, 1004s,941w, 798w.

Synthesis of [VO(TCPP-Zn_2-bpy)]·4DMF·4H_2O (1). [VO(TCPP)] (50 mg, 58 μmol), $Zn(NO_3)_2·6H_2O$ (35 mg, 116 μmol) and 4,4'-bipyridyl (18.1 mg, 116 μmol) were dissolved in 7 mL of DMF, and the solution placed in a glass capped vial. The solution was heated in oven at 80 °C for 24 h. After cooling, purple cubic-shape single-crystals were obtained. They were collected by filtration and washed with DMF and MeOH. Yield: 65 %. Elemental anal. calcd for $C_{70}H_{68}N_{10}O_{17}VZn_2$: C, 55.93; H, 4.56; N, 9.32; found: C, 56.11; H, 5.06; N, 9.48. FT-IR ($\tilde{\upsilon}_{max}/cm^{-1}$, KBr pellet): 3340w, 1630vs, 1548m, 1403vs, 1335w, 1204vw, 1180vw, 1069vw, 1007s,806m, 779m, 713w.

Synthesis of $VO_{0.05}TiO_{0.95}$(TCPP-Zn_2-bpy)] (1'). [VO(TCPP)] (2.0 mg 2.34 μmol) and [TiO(TCPP)] (64.5 mg 75.66 μmol) were mixed in 6 mL of DMF by using ultrasonication for 30 min. To the solution, $Zn(NO_3)_2·6H_2O$ (46.4 mg, 156 μmol) and 4,4'-bipyridyl (29.2 mg, 187.2 μmol) were added and placed in a glass capped vial. The solution was heated in oven at 80 °C for 24 h, and after cooling, purple cubic crystals of **1'** were obtained. They were collected by filtration and washed with DMF and MeOH. Yield: 57 %. Inductive coupled plasma atomic emission spectrometry (ICP-AES) was used to determine the effective concentration of V^{IV}:Ti^{IV}. This was found to be 4.94:95.06.

Synthesis of [VO(TPP)] (2). H_2TPP (0.25 g, 0.40 mmol) and [$VO(acac)_2$] (0.133 g, 0.50 mmol) were reacted at 180 °C in 6 mL of PhOH for 9 h. After that, the solvent was removed under vacuum and the residual solid was solubilized in CH_2Cl_2. A small portion of MeOH was added to the CH_2Cl_2 solution, inducing precipitation of **2** as a red-purple microcrystalline powder. The precipitate was washed several times with MeOH, then with Et_2O and air dried. Yield: 70 %. Compound **2** was recrystallized by slow evaporation of a CH_2Cl_2 solution, which gives purple shiny crystals suitable for X-ray analysis. Elemental anal. calcd for $C_{44}H_{28}N_4OV$: C, 77.76; H, 4.15; N, 8.24; found: C, 76.72; H, 4.36; N, 7.79. FT-IR ($\tilde{\upsilon}_{max}/cm^{-1}$, KBr pellet): 3130vw, 3111vw, 3024vw, 1831vw, 1595m, 1506w, 1487m, 1439m, 1337m, 1204m, 1175s, 1157m, 1070s, 1005vs, 835w, 806s, 750s, 725m, 702s, 661m, 527w, 453m.

Synthesis of [TiO(TPP)] (3). H_2TPP (0.50 g, 0.81 mmol) and [$TiO(acac)_2]_2$ (0.260 g, 0.50 mmol) were reacted at 180 °C in 12 mL of PhOH for 3 days. After that, the solvent was removed under vacuum and the residual solid was solubilized in CH_2Cl_2. A small portion of MeOH was added to the CH_2Cl_2 solution, inducing precipitation of **3** as a red-purple microcrystalline solid. The precipitate was washed several times with MeOH, then with Et_2O and air dried. Yield: 74

%. Compound **3** was recrystallized by slow evaporation of a CH_2Cl_2 solution, which gives purple shiny crystals suitable for X-ray analysis. Elemental anal. calcd for $C_{44}H_{28}N_4OTi$: C, 78.11; H, 4.17; N, 8.28; found: C, 77.54; H, 4.41; N, 7.79. FT-IR ($\bar{\upsilon}_{max}/cm^{-1}$, KBr pellet): 3130vw, 3111vw, 3024vw, 1831vw, 1595m, 1506w, 1483m, 1439m, 1335m, 1200m, 1175s, 1069s, 1157m, 1009vs, 979s, 966s, 835w, 806s, 748s, 723m, 702s, 660m, 525w, 438m.

Synthesis of $[VO_{0.02}TiO_{0.98}(TPP)]$ (2'). 2 (2.5 mg, 0.0037 mmol) and **3** (97.5 mg, 0.144 mmol) were dissolved in 50 mL of CH_2Cl_2. The solution was filtrated and 5 mL of MeOH were added, then the solvent was slowly evaporated under reduced pressure. **2'** precipitates as a red-purple microcrystalline solid, that was washed with MeOH, then Et_2O and air dried. Yield: quantitative. X-ray fluorescence (XRF) analysis was used to estimate the effective percentage of doping of V^{IV} by comparing the intensity of the XRF intensity of vanadium K_α emission of compound **2'** to a calibration curve obtained by mixing weighted amounts of the pure compounds (**2** and **3**) in the 1–20% concentration range. This was found to be 2(1)% of VO^{2+} and 98(1)% of TiO^{2+}.

Synthesis of $[VO_{0.30}TiO_{0.70}(TPP)]$ (2'''). Compound **2''** has been prepared according to the method described above for **2'** by recrystallization of a mixture of **2** (30.0 mg, 0.044 mmol) and **3** (70.0 mg, 0.103 mmol) in 75 mL of CH_2Cl_2. Yield: quantitative. Magnetic measurements were used to estimate the effective percentage of V^{IV} doping. This was found to be in agreement with the nominal content of VO^{2+} paramagnetic species (30(2)%).

Characterization. C, H, N analyses were performed with a *CHN-S Flash E1112 Thermofinnigan* analyzer. FT-IR spectra were performed on KBr pellets and collected with a *Shimadzu-8400S* spectrophotometer. X-ray fluorescence analyses were performed with a *WD-XRF Rigaku PrimusII* spectrophotometer. Inductive coupled plasma atomic emission spectrometry (ICP-AES) was performed at Research and Analytical Centre for Giant Molecules, Graduate school of Science, Tohoku University, Japan on a *SHIMADZU ICPE-9000* spectrometer with 5 % HNO_3 aqueous solution.

Single X-ray Crystallography. Single crystal X-ray diffraction measurements for compound **1** were performed on a ADSC Quantum210 installed in the Pohang Accelerator laboratory PLS-II beamlines. The synchrotron radiation was monochromated by using a double crystal monochromator (λ = 0.8000 Å). Single crystal X-ray diffraction measurements for **3** were performed on an *Oxford Xcalibur PX Ultra - Onyx CCD* diffractometer, using an Enhance Ultra

X-ray graphite-monochromated Cu$K\alpha$ (λ = 1.540 Å) radiation. The structures were solved by direct methods (SHELXL)[59] and refined on F^2 with full-matrix least squares (SHELXL), using the WinGX software package.[60] All non-H atoms were refined with anisotropic displacement parameters. Graphical material was prepared using Mercury CSD 3.9.[38] A summary of the crystallographic data and the structure refinement for compounds **1** and **3** is reported in Table 2.

Table 2. Summary of X-ray crystallographic data for **1** and **3**.

	1	**3**
Empirical formula	$C_{58}H_{32}N_6O_9VZn_2$	$C_{44}H_{28}N_4OTi$
Formula weight	1138.58	676.57
Crystal size, mm	0.20 × 0.20 × 0.20	0.50 × 0.30 × 0.15
Crystal system	Tetragonal	Tetragonal
Space group	*P4*	*I4*
a, *b* Å	16.644(2)	13.3796(2)
c, Å	13.854(2)	9.7766(3)
α,β, γ deg.	90	90
V, Å^3	3837.9(9)	1750.15(7)
Z	1	2
T, K	100(2)	100(2)
ρ (calcd), Mg/m^3	0.493	1.284
μ, mm^{-1}	0.391	2.385
θ range, deg.	0.81–50.00	5.61–72.51
GooF	1.074	1.037
*R*1	0.0879	0.0503
*wR*2	0.2547	0.1399

$R1 = \Sigma||F_o|-|F_c||/\Sigma|F_o|$, $wR2 = [\Sigma[w(F_o^2-F_c^2)^2]/\Sigma[w(F_o^2)^2]]^{½}$, $w = 1/[\sigma^2(F_o^2) + (aP)^2 + bP]$, where $P = [\max(F_o^2,0) + 2F_c^2]/3$.

Full crystallographic data for the solved structures have been deposited in the Cambridge Crystallographic Data Centre with CCDC numbers 1847868 (**1**), and 1849460 (**3**).

Powder X-ray Crystallography. Powder X-ray diffraction (PXRD) measurements on **1** and **1'** were performed on crushed polycrystalline samples by using an AFC-7R/ LW (Rigaku, Akishima, Japan) operated at 50 kV and 300 mA at 293 K. The data were collected in the diffraction angle range of 3–60° in steps of 0.02° with an irradiation time of 2 s/step. To prevent evaporation of the crystal solvent, the samples were loaded into a capillary (diameter: 0.8 mm, length: 80 mm, Hilgenderg, Malsfeld, Germany) with the mother liquor. Wide-Angle Powder

X-Ray Diffraction (PXRD) patterns on polycrystalline samples of **2**, **2'**, **3** were recorded on a *Bruker New D8 Advance DAVINCI* diffractometer in a theta-theta configuration equipped with a linear detector. The scans were collected within the range 5–40° (2θ) using CuK_α radiation (λ = 1.540 Å). Simulated patterns were generated from the atomic coordinates of the single-crystal structure solutions using the Mercury CSD 3.5 software[52] (copyright CCDC, http://www.ccdc.cam.ac.uk/mercury/) using a FWHM (full width at half maximum) of 0.10 and a 2θ step of 0.025.

Magnetic Measurements. Magnetic susceptibility measurements were performed by using a *Quantum Design Physical Property Measurement System* (PPMS). Alternate current susceptibility measurements were performed in the frequency (ν) range 10–10000 Hz in the temperature range 2.0−50 K by applying an oscillating field of 10 Oe and applied static magnetic fields up to 8.5 T. Measurements were performed on randomly oriented powder samples of **1** (37.12 mg), **2** (51.68 mg) and **2''** (45.38 mg). Susceptibility data were corrected for the sample holder previously measured using the same conditions and for the diamagnetic contributions as deduced by using Pascal's constant tables.[61]

THz time-domain spectroscopy set-up. THz spectra were measured by time-domain transmission spectroscopy using a table-top experimental set-up equipped with optical laser pulses (T-light 780 nm fiber laser, MenloSystems) and low-temperature GaAs photoconductive antennas. Low temperatures measurements are allowed by means of a closed-cycle Helium cryostat in the temperature range from 20 to 300 K. The developed acquisition procedure enables to achieve a signal-to-noise ratio higher than what is commonly achieved in standard far-infrared investigations. The accurate analysis of the data enables to disentangle the signals from spurious contributions coming from multiple reflections. The detailed description of the experimental set-up and the data analysis procedure is reported elsewhere.[62,63] The spectra were measured in pellets of 13.2 mm diameter and thickness of about 0.7 mm. These were made by pressing under a manual hydraulic press (~ 0.8 GPa) a mixture of microcrystals and polyethylene powder (Merck).

Electron Paramagnetic Resonance. CW X-Band EPR spectra of all samples were recorded on a *Bruker Elexsys E500* spectrometer equipped with a SHQ cavity ($\nu \cong$ 9.70 GHz). Low temperature measurements were obtained using an *Oxford Instruments ESR900* continuous flow helium cryostat and the temperature controlled by an Oxford Instrument ITC. Pulsed EPR measurements were carried out with a *Bruker Elexsys E580* at X-band ($\nu \cong$ 9.70 GHz) equipped

with a flexline dielectric ring ENDOR resonator (*Bruker EN 4118X-MD4*). Temperatures between 4.5 and 250 K were obtained with *an Oxford Instruments CF935* continuous flow helium cryostat. *Echo detected field swept EPR* spectra were recorded by using the Hahn Echo pulse sequence ($\pi/2$—τ—π—τ—*echo*) with fixed interpulse delay time τ = 200 ns, $t_{\pi/2}$ = 16 ns and t_{π} = 32 ns. *Phase memory times* were measured by the Hahn Echo sequence upon increasing the interpulse delay τ starting from τ = 98 ns. Typical pulse lengths were $t_{\pi/2}$ = 40 ns and t_{π}= 80 ns. *Spin-lattice relaxation times* were measured using the standard inversion recovery sequence (π—t_d—$\pi/2$—τ—π—τ—*echo*), with $\pi/2$ = 16 ns. The uncertainty in T_1 estimated from replicate measurements was 5%–10% depending upon the signal-to-noise ratio at a given temperature-field combination. *Nutation measurements* were performed with a nutation pulse (t_p) of variable length followed by a Hahn echo sequence (t_p—t_d—$\pi/2$—τ— π —τ—*echo*) with $t_d >> T_m$ (*i.e.* t_d = 7 μs for 4 K and 2 μs for room temperature measurements). The interpulse delay τ was 200 ns and the pulse length of the detection sequence was adjusted depending on the attenuation level of B_1. *Hyperfine Sublevel Correlation* (HYSCORE) experiments[64] were carried out with the pulse sequence $\pi/2$–τ–$\pi/2$–τ_1–π–τ_2–$\pi/2$–τ –*echo* with the microwave pulse length $t_{\pi/2}$ = 16 ns and t_{π} = 16 ns. The time intervals t_1 and t_2 were varied in steps of 8 ns starting from 96 ns to 2704 ns. Spectra with two τ values (100 ns and 136 ns), which are specified in the figure captions where recorded to avoid blind spot effects. An eight-step phase cycle was used for eliminating unwanted echoes. The time traces of the HYSCORE spectra were baseline corrected with a third-order polynomial, apodized with a Hamming window and zero filled. After two-dimensional Fourier transformation, the absolute value spectra were calculated. The HYSCORE frequencies were computed for a three-spin system (S = 1/2, I_a = 1, I_b = 1) using the *endorfrq* function, implemented in the Easyspin program.[47]

ASSOCIATED CONTENT

Supporting Information

The Supporting Information is available free of charge on the ACS Publications website at DOI: XXXXX. Additional figures, PXRD patterns, magnetic susceptibility and HYSCORE data, as mentioned in the text.

AUTHOR INFORMATION

Corresponding Authors

*E-mail: roberta.sessoli@unifi.it

*E-mail: yamasita.m@gmail.com

Notes

The authors declare no competing financial interest.

ACKNOWLEDGMENTS

This work was performed with the financial support of the Italian MIUR through the project PRIN 2015-HYFSRT, Fondazione Ente Cassa di Risparmio di Firenze, European Project SUMO (QuantERA call 2017), and the Photon Factory Program Advisory Committee (Proposal No. 2016G040, beamline NW2A). European COST Action CA15128 MOLSPIN is also acknowledged. M.Y. thanks the support by the 111 project (B18030) from China. We thank Sandra and Gareth Eaton (University of Denver, Colorado, U.S.A.) for the stimulating discussions.

REFERENCES

(1) Nielsen, M. A.; Chuang, I. L. *Quantum Computation and Quantum Information*; Cambridge University Press: Cambridge, 2010.

(2) Schirhagl, R.; Chang, K.; Loretz, M.; Degen, C. L. Nitrogen-Vacancy Centers in Diamond: Nanoscale Sensors for Physics and Biology. *Annu. Rev. Phys. Chem.* **2014**, *65*, 83–105.

(3) Wu, Y.; Jelezko, F.; Plenio, M. B.; Weil, T. Diamond Quantum Devices in Biology. *Angew. Chemie Int. Ed.* **2016**, *55*, 6586–6598.

(4) Degen, C. L.; Reinhard, F.; Cappellaro, P. Quantum Sensing. *Rev. Mod. Phys.* **2017**, *89*, 035002.

(5) Knill, E.; Laflamme, R.; Milburn, G. J. A Scheme for Efficient Quantum Computation with Linear Optics. *Nature* **2001**, *409*, 46–52.

(6) Blatt, R.; Wineland, D. Entangled States of Trapped Atomic Ions. *Nature* **2008**, *453*, 1008–1015.

(7) Mi, X.; Benito, M.; Putz, S.; Zajac, D. M.; Taylor, J. M.; Burkard, G.; Petta, J. R. A Coherent Spin–Photon Interface in Silicon. *Nature* **2018**, *555*, 599–603.

(8) Clarke, J.; Wilhelm, F. K. Superconducting Quantum Bits. *Nature* **2008**, *453*, 1031–1042.

(9) Kennedy, T. A.; Colton, J. S.; Butler, J. E.; Linares, R. C.; Doering, P. J. Long Coherence Times at 300 K for Nitrogen-Vacancy Center Spins in Diamond Grown by Chemical Vapor Deposition. *Appl. Phys. Lett.* **2003**, *83*, 4190–4192.

(10) Balasubramanian, G.; Neumann, P.; Twitchen, D.; Markham, M.; Kolesov, R.; Mizuochi, N.; Isoya, J.; Achard, J.; Beck, J.; Tissler, J.; Jacques, V.; Hemmer, P. R.; Jelezko, F.; Wrachtrup, J. Ultralong Spin Coherence Time in Isotopically Engineered Diamond. *Nat. Mater.* **2009**, *8*, 383–387.

(11) Bar-Gill, N.; Pham, L. M.; Jarmola, A.; Budker, D.; Walsworth, R. L. Solid-State Electronic Spin Coherence Time Approaching One Second. *Nat. Commun.* **2013**, *4*, 1743.

(12) Ardavan, A.; Rival, O.; Morton, J. J. L.; Blundell, S. J.; Tyryshkin, A. M.; Timco, G. A.; Winpenny, R. E. P. Will Spin-Relaxation Times in Molecular Magnets Permit Quantum Information Processing? *Phys. Rev. Lett.* **2007**, *98*, 057201.

(13) Tesi, L.; Lucaccini, E.; Cimatti, I.; Perfetti, M.; Mannini, M.; Atzori, M.; Morra, E.; Chiesa, M.; Caneschi, A.; Sorace, L.; Sessoli, R. Quantum Coherence in a Processable Vanadyl Complex: New Tools for the Search of Molecular Spin Qubits. *Chem. Sci.* **2016**, *7*, 2074–2083.

(14) Troiani, F.; Affronte, M. Molecular Spins for Quantum Information Technologies. *Chem. Soc. Rev.* **2011**, *40*, 3119.

(15) Aromí, G.; Aguilà, D.; Gamez, P.; Luis, F.; Roubeau, O. Design of Magnetic Coordination Complexes for Quantum Computing. *Chem. Soc. Rev.* **2012**, *41*, 537–546.

(16) Atzori, M.; Morra, E.; Tesi, L.; Albino, A.; Chiesa, M.; Sorace, L.; Sessoli, R. Quantum Coherence Times Enhancement in Vanadium(IV)-Based Potential Molecular Qubits: The Key Role of the Vanadyl Moiety. *J. Am. Chem. Soc.* **2016**, *138*, 11234–11244.

(17) Warner, M.; Din, S.; Tupitsyn, I. S.; Morley, G. W.; Stoneham, A. M.; Gardener, J. A.; Wu, Z.; Fisher, A. J.; Heutz, S.; Kay, C. W. M.; Aeppli, G. Potential for Spin-Based Information Processing in a Thin-Film Molecular Semiconductor. *Nature* **2013**, *503*, 504–508.

(18) Bader, K.; Dengler, D.; Lenz, S.; Endeward, B.; Jiang, S.-D.; Neugebauer, P.; van

Slageren, J. Room Temperature Quantum Coherence in a Potential Molecular Qubit. *Nat. Commun.* **2014**, *5*, 5304.

(19) Zadrozny, J. M.; Niklas, J.; Poluektov, O. G.; Freedman, D. E. Multiple Quantum Coherences from Hyperfine Transitions in a Vanadium(IV) Complex. *J. Am. Chem. Soc.* **2014**, *136*, 15841–15844.

(20) Zadrozny, J. M.; Niklas, J.; Poluektov, O. G.; Freedman, D. E. Millisecond Coherence Time in a Tunable Molecular Electronic Spin Qubit. *ACS Cent. Sci.* **2015**, *1*, 488–492.

(21) Graham, M. J.; Yu, C.-J.; Krzyaniak, M. D.; Wasielewski, M. R.; Freedman, D. E. Synthetic Approach To Determine the Effect of Nuclear Spin Distance on Electronic Spin Decoherence. *J. Am. Chem. Soc.* **2017**, *139*, 3196–3201.

(22) Atzori, M.; Benci, S.; Morra, E.; Tesi, L.; Chiesa, M.; Torre, R.; Sorace, L.; Sessoli, R. Structural Effects on the Spin Dynamics of Potential Molecular Qubits. *Inorg. Chem.* **2018**, *57*, 731–740.

(23) Gao, W.-Y.; Chrzanowski, M.; Ma, S. Metal–Metalloporphyrin Frameworks: A Resurging Class of Functional Materials. *Chem. Soc. Rev.* **2014**, *43*, 5841–5866.

(24) Furukawa, H.; Cordova, K. E.; O'Keeffe, M.; Yaghi, O. M. The Chemistry and Applications of Metal-Organic Frameworks. *Science* **2013**, *341*, 1230444.

(25) Huh, S.; Kim, S.-J.; Kim, Y. Porphyrinic Metal–Organic Frameworks from Custom-Designed Porphyrins. *CrystEngComm* **2016**, *18*, 345–368.

(26) Yi, F.-Y.; Chen, D.; Wu, M.-K.; Han, L.; Jiang, H.-L. Chemical Sensors Based on Metal-Organic Frameworks. *Chempluschem* **2016**, *81*, 675–690.

(27) Kreno, L. E.; Leong, K.; Farha, O. K.; Allendorf, M.; Van Duyne, R. P.; Hupp, J. T. Metal–Organic Framework Materials as Chemical Sensors. *Chem. Rev.* **2012**, *112*, 1105–1125.

(28) Chen, B.; Xiang, S.; Qian, G. Metal−Organic Frameworks with Functional Pores for Recognition of Small Molecules. *Acc. Chem. Res.* **2010**, *43*, 1115–1124.

(29) Urtizberea, A.; Natividad, E.; Alonso, P. J.; Andrés, M. A.; Gascón, I.; Goldmann, M.; Roubeau, O. A Porphyrin Spin Qubit and Its 2D Framework Nanosheets. *Adv. Funct. Mater.* **2018**, *28*, 1801695.

(30) Zadrozny, J. M.; Gallagher, A. T.; Harris, T. D.; Freedman, D. E. A Porous Array of

Clock Qubits. *J. Am. Chem. Soc.* **2017**, *139*, 7089–7094.

(31) Escalera-Moreno, L.; Suaud, N.; Gaita-Ariño, A.; Coronado, E. Determining Key Local Vibrations in the Relaxation of Molecular Spin Qubits and Single-Molecule Magnets. *J. Phys. Chem. Lett.* **2017**, *8*, 1695–1700.

(32) Atzori, M.; Tesi, L.; Benci, S.; Lunghi, A.; Righini, R.; Taschin, A.; Torre, R.; Sorace, L.; Sessoli, R. Spin Dynamics and Low Energy Vibrations: Insights from Vanadyl-Based Potential Molecular Qubits. *J. Am. Chem. Soc.* **2017**, *139*, 4338–4341.

(33) Escalera-Moreno, L.; Baldoví, J. J.; Gaita-Ariño, A.; Coronado, E. Spin States, Vibrations and Spin Relaxation in Molecular Nanomagnets and Spin Qubits: A Critical Perspective. *Chem. Sci.* **2018**, *9*, 3265–3275.

(34) Atzori, M.; Tesi, L.; Morra, E.; Chiesa, M.; Sorace, L.; Sessoli, R. Room-Temperature Quantum Coherence and Rabi Oscillations in Vanadyl Phthalocyanine: Toward Multifunctional Molecular Spin Qubits. *J. Am. Chem. Soc.* **2016**, *138*, 2154–2157.

(35) Barron, P. M.; Son, H.-T.; Hu, C.; Choe, W. Highly Tunable Heterometallic Frameworks Constructed from Paddle-Wheel Units and Metalloporphyrins. *Cryst. Growth Des.* **2009**, *9*, 1960–1965.

(36) Goldberg, I. Crystal Engineering of Porphyrin Framework Solids. *Chem. Commun.* **2005**, 1243.

(37) Feng, D.; Gu, Z.-Y.; Li, J.-R.; Jiang, H.-L.; Wei, Z.; Zhou, H.-C. Zirconium-Metalloporphyrin PCN-222: Mesoporous Metal-Organic Frameworks with Ultrahigh Stability as Biomimetic Catalysts. *Angew. Chemie Int. Ed.* **2012**, *51*, 10307–10310.

(38) Macrae, C. F.; Edgington, P. R.; McCabe, P.; Pidcock, E.; Shields, G. P.; Taylor, R.; Towler, M.; van de Streek, J. Mercury : Visualization and Analysis of Crystal Structures. *J. Appl. Crystallogr.* **2006**, *39*, 453–457.

(39) Cole, K. S.; Cole, R. H. Dispersion and Absorption in Dielectrics I. Alternating Current Characteristics. *J. Chem. Phys.* **1941**, *9*, 341–351.

(40) Van Vleck, J. H. Paramagnetic Relaxation and the Equilibrium of Lattice Oscillators. *Phys. Rev.* **1941**, *59*, 724–729.

(41) Scott, P. L.; Jeffries, C. D. Spin-Lattice Relaxation in Some Rare-Earth Salts at Helium Temperatures; Observation of the Phonon Bottleneck. *Phys. Rev.* **1962**, *127*, 32–51.

(42) Tesi, L.; Lunghi, A.; Atzori, M.; Lucaccini, E.; Sorace, L.; Totti, F.; Sessoli, R. Giant Spin–Phonon Bottleneck Effects in Evaporable Vanadyl-Based Molecules with Long Spin Coherence. *Dalt. Trans.* **2016**, *45*, 16635–16643.

(43) Standley, K. J.; Vaughan, R. A. *Electron Spin Relaxation Phenomena in Solids*; Springer US: Boston, MA, 1969.

(44) Gómez-Coca, S.; Urtizberea, A.; Cremades, E.; Alonso, P. J.; Camón, A.; Ruiz, E.; Luis, F. Origin of Slow Magnetic Relaxation in Kramers Ions with Non-Uniaxial Anisotropy. *Nat. Commun.* **2014**, *5*, 4300.

(45) Van Vleck, J. H. Paramagnetic Relaxation Times for Titanium and Chrome Alum. *Phys. Rev.* **1940**, *57*, 426–447.

(46) De Vroomen, A. C.; Lijphart, E. E.; Prins, D. Y. H.; Marks, J.; Poulis, N. J. Electron Spin-Lattice Relaxation of the Zeeman and Interaction Systems in CuCs2(SO4)2·6H2O. *Physica* **1972**, *61*, 241–249.

(47) Stoll, S.; Schweiger, A. EasySpin, a Comprehensive Software Package for Spectral Simulation and Analysis in EPR. *J. Magn. Reson.* **2006**, *178*, 42–55.

(48) Gourier, D.; Delpoux, O.; Bonduelle, A.; Binet, L.; Ciofini, I.; Vezin, H. EPR, ENDOR, and HYSCORE Study of the Structure and the Stability of Vanadyl−Porphyrin Complexes Encapsulated in Silica: Potential Paramagnetic Biomarkers for the Origin of Life. *J. Phys. Chem. B* **2010**, *114*, 3714–3725.

(49) Moons, H.; Patel, H. H.; Gorun, S. M.; Doorslaer, S. Van. Electron Paramagnetic Resonance and DFT Analysis of the Effects of Bulky Perfluoroalkyl Substituents on a Vanadyl Perfluoro Phthalocyanine. *Z. Phys. Chem.* **2017**, *231*, 887–903.

(50) Eaton, S. S.; Eaton, G. R. *Distance Measurements in Biological Systems by EPR*; Berliner, L. J., Eaton, G. R., Eaton, S. S., Eds.; Biological Magnetic Resonance; Springer US: Boston, MA, 2002; Vol. 19.

(51) Du, J.-L.; Eaton, G. R.; Eaton, S. S. Electron Spin Relaxation in Vanadyl, Copper(II), and Silver(II) Porphyrins in Glassy Solvents and Doped Solids. *J. Magn. Reson. Ser. A* **1996**, *119*, 240–246.

(52) Domke, K. F.; Pettinger, B. In Situ Discrimination between Axially Complexed and Ligand-Free Co Porphyrin on Au(111) with Tip-Enhanced Raman Spectroscopy. *ChemPhysChem* **2009**, *10*, 1794–1798.

(53) Li, D.; Peng, Z.; Deng, L.; Shen, Y.; Zhou, Y. Theoretical Studies on Molecular Structure and Vibrational Spectra of Copper Phthalocyanine. *Vib. Spectrosc.* **2005**, *39*, 191–199.

(54) Kincaid, J.; Nakamoto, K. Vibrational Spectra of Transition Metal Complexes of Tetraphenylporphine. *J. Inorg. Nucl. Chem.* **1975**, *37*, 85–89.

(55) Jee, B.; Eisinger, K.; Gul-E-Noor, F.; Bertmer, M.; Hartmann, M.; Himsl, D.; Pöppl, A. Continuous Wave and Pulsed Electron Spin Resonance Spectroscopy of Paramagnetic Framework Cupric Ions in the Zn(II) Doped Porous Coordination Polymer $Cu_{3-x}Zn_x(btc)_2$. *J. Phys. Chem. C* **2010**, *114*, 16630–16639.

(56) Poryvaev, A. S.; Sheveleva, A. M.; Demakov, P. A.; Arzumanov, S. S.; Stepanov, A. G.; Dybtsev, D. N.; Fedin, M. V. Pulse EPR Study of Gas Adsorption in Cu^{2+}-Doped Metal–Organic Framework $[Zn_2(1,4\text{-bdc})_2(dabco)]$. *Appl. Magn. Reson.* **2018**, *49*, 255–264.

(57) Šimėnas, M.; Macalik, L.; Aidas, K.; Kalendra, V.; Klose, D.; Jeschke, G.; Mączka, M.; Völkel, G.; Banys, J.; Pöppl, A. Pulse EPR and ENDOR Study of Manganese Doped $[(CH_3)_2NH_2][Zn(HCOO)_3]$ Hybrid Perovskite Framework. *J. Phys. Chem. C* **2017**, *121*, 27225–27232.

(58) Müller, H.-E.; Völkel, G.; Brunner, W.; Cevc, P.; Kurkin, I. N. Electron Spin Relaxation in Ferroelastic $KH_3(SeO_3)_2$. *Phys. status solidi* **1987**, *141*, 343–349.

(59) Sheldrick, G. M. Crystal Structure Refinement with SHELXL. *Acta Crystallogr. Sect. C Struct. Chem.* **2015**, *71*, 3–8.

(60) Farrugia, L. J. WinGX and ORTEP for Windows : An Update. *J. Appl. Crystallogr.* **2012**, *45*, 849–854.

(61) Bain, G. A.; Berry, J. F. Diamagnetic Corrections and Pascal's Constants. *J. Chem. Educ.* **2008**, *85*, 532.

(62) Tasseva, J.; Taschin, A.; Bartolini, P.; Striova, J.; Fontana, R.; Torre, R. Thin Layered Drawing Media Probed by THz Time-Domain Spectroscopy. *Analyst* **2017**, *142*, 42–47.

(63) Taschin, A.; Bartolini, P.; Tasseva, J.; Torre, R. THz Time-Domain Spectroscopic Investigations of Thin Films. *Measurement* **2018**, *118*, 282–288.

(64) Höfer, P.; Grupp, A.; Nebenführ, H.; Mehring, M. Hyperfine Sublevel Correlation (Hyscore) Spectroscopy: A 2D ESR Investigation of the Squaric Acid Radical. *Chem. Phys. Lett.* **1986**, *132*, 279–282.